Artefacts of isotropic inversion applied to magnetotelluric data from an anisotropic Earth

Marion P. Miensopust[1,2] and Alan G. Jones[1]

[1]*Dublin Institute for Advanced Studies, School of Cosmic Physics, Dublin, Ireland. E-mail: marion@cp.dias.ie*
[2]*Institut für Geophysik, Westfälische Wilhelms-Universität Münster, Germany*

SUMMARY

2-D isotropic approaches are standard for magnetotelluric (MT) data modelling and inversion. Unfortunately, the real subsurface structure is not isotropic everywhere and one should be aware of the possible consequences of applying an isotropic inversion to data from an anisotropic Earth. The work presented herein was motivated by discovering an unusual mid- to lower-crust conductor that appeared to be bent downward into the lithospheric mantle, compared to the neighbouring terranes, when applying routine 2-D isotropic inversion. One major difference between the terranes is the presence of the Okavango giant mafic dyke swarm (northeastern Botswana), beneath which the conductor is imaged to be in the lithospheric mantle rather than the lower crust. The limited width of the dykes makes them an anisotropic feature rather than a normal 2-D structure at MT scale. To examine the possible effects of the dykes, synthetic data were generated from an 1-D model, accounting for the dyke swarm by using an anisotropic block, and then inverted isotropically. The synthetic tests showed that the normal 2-D decomposition and strike analysis techniques are not removing these large scale anisotropic effects, and that an isotropic inversion result obtained in the presence of an anisotropic structure has to be treated with caution. The comparison of the synthetic data with the presented case history strongly suggests that the lithospheric depths of the conductor is an artefact, and it is most likely located in the lower-crust, as everywhere else in the area. Focused anisotropic inversion of the dyke swarm area supports the assumption of a crustal anisotropic structure related to the Okavango Dyke Swarm that affects the isotropic inversion results.

Key words: Electrical anisotrophy; Electrical properties; Electromagnetic theory; Magnetotelluric; Geomagnetic induction.

1 INTRODUCTION

Modelling and inversion tools for magnetotelluric (MT) data are based on a number of assumptions, one of which is often isotropic resistivity within each cell (layer or block). For 2-D approaches data are often treated by decomposition and strike analysis techniques, as for example the program *strike* by McNeice & Jones (2001), before modelling. Based on the Groom-Bailey decomposition (Bailey & Groom 1987; Groom & Bailey 1989), *strike* analyses electric field galvanic distortions present and determines the most consistent geoelectric, regional strike direction of a data set valid for most sites at most periods. The galvanic distortion comprises the effects of near-surface, small-scale heterogeneities in the resistivity distribution physically separated as *twist*, *shear*, *distortion anisotropy* and a scaling factor called *gain*. These effects (except for the gain) are removed by applying *strike* to the data, and results in 2-D regional response curves which can then be inverted using standard modelling tools.

Although the resistivity might be isotropic on the microscale (i.e. no intrinsic anisotropy at the grain or fabric scale), bulk anisotropy

might be present on a larger scale if the averaging volume comprises preferred orientations, such as, for example dykes, layering or lamination (Eisel & Haak 1999; Weidelt 1999; Wannamaker 2005). Preferred orientations of fracture porosity, lithologic layering and oriented heterogeneity are the sources of upper crustal anisotropy, whereas macroscale elements, such as fluidized/melt-bearing or graphitized shear zones or deformed metasedimentary belt units, tend to cause enhanced conductivity along the strike direction of the structure and are the most common causes of lower crustal anisotropy (Wannamaker 2005). In the upper mantle, the same sources of anisotropy as in the lower crust are possible, and additionally there is the possibility of strong electrical anisotropy due to hydrous defects within shear-aligned olivine crystals (Wannamaker 2005) and the recently-reported possibility of anisotropic melt geometry in strong strain fields (Caricchi *et al.* 2011). Numerous MT field examples inferred electrical anisotropy at lower crustal and lithospheric mantle depths (e.g. Kellett *et al.* 1992; Eisel & Bahr 1993; Kurtz *et al.* 1993; Mareschal *et al.* 1995; Wannamaker 1997; Davey *et al.* 1998; Eisel & Haak 1999; Bahr & Simpson 2002; Leibecker *et al.* 2002; Eaton *et al.* 2004;
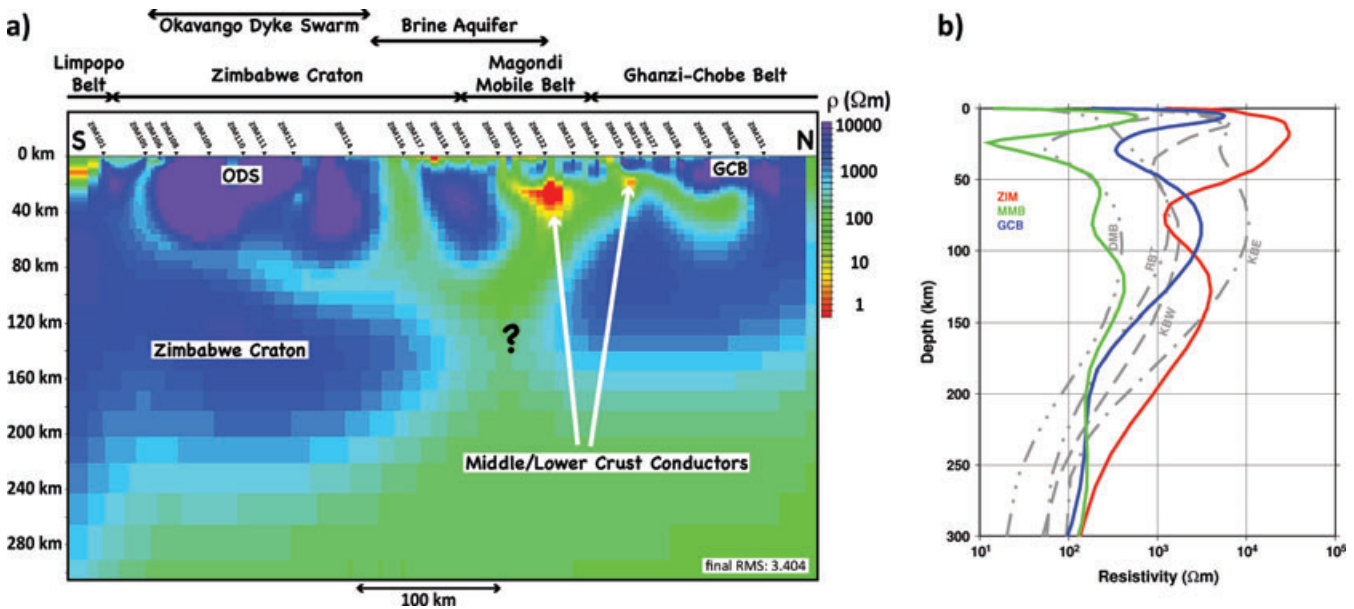
Figure 1. The 2D smooth inversion model (vertical exaggeration = 1.0) from the so-called ZIM line in northeastern Botswana in relation to the known surface extent of geological terranes (a) and average resistivity-depth profiles (b). The arrows above the image of the resistivity structure (a) show the crustal extents of the Limpopo Belt, Zimbabwe Craton, Magondi Mobile Belt and Ghanzi-Chobe Belt (GCB) with respect to MT sites of the ZIM line, adapted from the regional scale geological terrane boundaries based on potential field data (Webb 2009). The extent of the Okavango Dyke Swarm (ODS), known from magnetic data, is indicated, as well as an estimated extent of the brine aquifer related to the Makgadikgadi salt pan complex. The dominant resistivity features related to the main geological terranes are labelled and the question mark indicates the area of missing data coverage. In addition, average resistivity-depth profiles (b) of the main terrane of the ZIM profile (ZIM, Zimbabwe Craton; MMB, Magondi Mobile Belt; GCB, Ghanzi-Chobe Belt) are shown in comparison to other terranes in Southern Africa (DMB, Damara Mobile Belt; RBT, Rehoboth Terrane; KBE and KBW Eastern and Western Kimberley Block; Muller *et al.* 2009). Although the Zimbabwe Craton (red) shows an enhanced conductivity in the upper lithospheric mantle, most other resistivity-depth profiles indicate a lower resistivity in the mid to lower crust. Taken from Miensopust *et al.* (2011).

Wannamaker *et al.* 2004; Gatzemeier & Moorkamp 2005; Baba *et al.* 2006; Hamilton *et al.* 2006; Padilha *et al.* 2006; Brasse *et al.* 2009). MT data are very sensitive to anisotropic structures and their spatial distribution, which challenges the modelling, inversion and interpretation tools available. Heise *et al.* (2006) investigated phase splits in MT data in the presence of anisotropy using the phase tensor approach by Caldwell *et al.* (2004) and their forward modelling showed that for the models they studied the phase split is a result of the interface between the isotropic and anisotropic material rather than of the anisotropy itself. Therefore, a phase split is not a sufficient condition to identify anisotropy. Nevertheless, anomalous phases exceeding 90° that cannot be modelled using isotropic 1-D or 2-D approaches can be explained by the presence of two anisotropic structures of oblique (obliquity greater than 70°, maximum phases when perpendicular) anisotropy strike directions (Heise & Pous 2003; Weckmann *et al.* 2003). Heise & Pous (2003) performed a thorough investigation of the influence of the anisotropy strike direction, anisotropy contrast, geometry of the anisotropic block and the angle between the two anisotropic structures on the MT responses, and presented arguably the first convincing case for anisotropy in the lower crust. Although some forward modelling and inversion tools considering anisotropy are available to investigate MT data, for example a 1-D anisotropy forward modelling and inversion program by Pek & Santos (2002), the 2-D forward modelling code by Pek & Verner (1997), a 2-D inversion algorithm based on the code by Rodi & Mackie (2001) (first used by Baba *et al.* 2006), these tools are not applied routinely. Electrical anisotropy is far more likely to be present (especially upper crustal rocks can be highly anisotropic) than currently interpreted, and neglecting its effects is likely to have led to erroneous interpretations.

As part of the Southern African MagnetoTelluric EXperiment (SAMTEX), the so-called ZIM (Zimbabwe Craton) profile in northeastern Botswana, running mainly parallel to the Botswanan–Zimbabwean border, was interpreted based on 2-D isotropic inversions of the observed MT data with a site spacing of approximately 20 km (Miensopust 2010; Miensopust *et al.* 2011). The ZIM profile crosses the extensive Okavango Dyke Swarm and the 2-D isotropic inversion results (Fig. 1a), and average resistivity-depth profiles of different terranes (Fig. 1b), showed an unusual less-resistive feature at uppermost lithospheric mantle depths beneath the dyke swarm, whereas in almost all surrounding terranes a conductor was found in the mid- to lower-crust (Muller *et al.* 2009; Miensopust 2010; Miensopust *et al.* 2011).

The Okavango Dyke Swarm, together with the Save-Limpopo and the Olifants River Dyke Swarms, form the so-called Nuanetsi Triple Junction that is not a structure of Jurassic origin alone, but reflects weakened lithospheric pathways (pre-existing ancient basement structures) that have controlled dyke orientation over hundreds of millions of years (Jourdan *et al.* 2006). The 110°-trending (Jourdan *et al.* (2006): 109° ± 12°E of N) giant Okavango Dyke Swarm extends over a 1500 km strike length through Archaean basement terranes and Permo-Jurassic sedimentary sequences. The dykes are mainly coarse-grained dolerites (Elburg & Goldberg 2000; Aubourg *et al.* 2008), which are hosted by granites, gneiss and amphibolites in the Francistown area (Aubourg *et al.* 2008). ^{40}Ar/^{39}Ar age determinations by Elburg & Goldberg (2000) and Le Gall *et al.* (2002) show that the dykes are about 178.4 ± 1.1 Ma to 179.3 ± 1.2 Ma in age, but they also identify one dyke in the swarm as Proterozoic in age. Jourdan *et al.* (2004) broadened the range of emplacement ages of the Karoo dykes to between 178.4 ± 1.1 Ma to 180.9 ± 1.3 Ma,

with a probability peak at 179 Ma. They also identified eight Proterozoic dykes and three Proterozoic sills with ages of 850–1700 Ma. Jourdan *et al.* (2004) suggested, based on the relationships between the age and geochemical composition, that the Okavango Dyke Swarm includes at least 10% of Proterozoic dykes located in the central part of the Jurassic swarm. Therefore, they concluded that the Nuanesti Triple Junction is an inherited Proterozoic structure that was reactivated during Jurassic times. Le Gall *et al.* (2005) studied the dyke swarm and the geometry and distribution of individual dykes within the swarm in more detail. They found that about 70% of the dykes are within 10° of parallelism with the 110°E of N trend of the swarm envelop, that the Karoo dyke length ranges from 1 to 18 km, and that about 91% of the dykes are vertical, the other 9% are within 30° of vertical. Their determined range of dyke widths is from 0.2 to 69 m based on field measurements (mapping outcrops in the river bed of the Shashe River near Francistown, which is in proximity to the ZIM profile), and 11 to 69 m from magnetic data. The arithmetic mean dyke width is about 17 m based on the magnetic measurements and about 16 m from the field measurements. Le Gall *et al.* (2005) also investigated the gradual westerly narrowing of the high density zone of the Okavango Dyke Swarm, from 60 km in the Francistown area to 53 and 45 km in the Maun (about 400 km northwest) and Ngami (about 200 km further northwest) areas, respectively. Also the dyke spacing increases from 300 m (Francistown) to 1.5 km (Maun/Ngami), and, therefore, crustal dilatation decreases from 12.2% (Francistown) to 2.6% (Maun/Ngami). Le Gall *et al.* (2005) suggested that such a change in lateral distribution of dykes, coupled with lack of map-scaled deflection of the swarm trend around magma chambers at depth, can be explained by the Karoo mafic dykes propagating laterally westwards, away from the Nuanetsi source region, instead of being injected vertically from deep-seated linear magmatic ridges. The model of lateral flow of Karoo magma is also supported by the anisotropy of magnetic susceptibility (AMS) data that show a transition from predominantly vertical (near the Nuametsi source region) to horizontal magma flow with increasing distance from the Nuanetsi focal point (Tshoso 2003; Le Gall *et al.* 2005; Aubourg *et al.* 2008).

The Okavango Dyke Swarm (mainly) consists of Karoo-aged dolerite dykes (Elburg & Goldberg 2000; Aubourg *et al.* 2008). Based on deep electrical soundings investigating the Karoo Supergroup in South Africa, van Zijl (2006) estimates that the dolerites have an average resistivity of 30 000 Ωm, as determined exclusively from soundings close to, or at, the sites of deep boreholes, where the distribution and thickness of the dolerites and hosting sediments were known. The dyke swarm is therefore a resistive structure and, as the dykes are, on average, 16–17 m wide (Le Gall *et al.* 2005), they cannot be individually resolved and are more an anisotropic feature than a normal 2-D structure at the MT scale.

This raises the question, could the lithospheric mantle conductor imaged beneath them be an artefact of isotropic inversion applied to data measured above an anisotropic structure? To date, no feasibility study has been undertaken to investigate how well a resistivity structure is recovered by an isotropic inversion if large scale anisotropy is present that does not vanish when 2-D-based decomposition and strike analysis techniques are applied. Therefore, based on the dyke swarm scenario synthetic test models were designed and the normal procedures of data processing, analysis and 2-D isotropic inversion were applied to the synthetic data set and compared to the inversion results of the real data set. In addition, 2-D inversion for anisotropic structure, based on the assumption of anisotropy aligned with the inversion mesh axes, was conducted and also compared to the other

results. Finally, the part of the ZIM profile above the dyke swarm was inverted anisotropically.

2 SYNTHETIC TESTS

2.1 Model design, derivation and analysis of synthetic responses

The 2-D synthetic tests were performed using relatively simple models based on an 1-D, layered background. The layered background was chosen to be similar to the resistivity distribution found in the area of the Archaean Zimbabwe Carton, where the data of the case history (Fig. 1) were observed. In the background model the upper crust, down to 25 km, is moderately resistive (1000 Ωm) whereas the lower crust, from 25 to 35 km, is a more conducting layer of 100 Ωm. The resistive, deep lithospheric mantle root of the craton is represented by a layer of 2000 Ωm down to 210 km depth. Below 210 km a homogeneous half-space of 100 Ωm is assumed (representing the asthenosphere). This layered background model will be referred to as base model (Fig. 2a).

Anisotropy was introduced to either the upper crustal layer (blue dashed line in Fig. 2b) or both crustal layers (red dashed line in Fig. 2b). The anisotropic resistivity matrix can be diagonalized and expressed by three principle resistivity values (i.e. main diagonal elements of the diagonalized matrix) and a rotation matrix described by the three angles of the anisotropic strike, slant and dip directions (Weidelt 1999; Pek & Santos 2002). The principle resistivities for anisotropy have been approximated using Kirchhoff's Law for parallel and serial connections based on the scenario of the case history, where a dyke swarm (dyke resistivities approximately 30 000 Ωm; van Zijl 2006) with 12.2% dilatation (Le Gall *et al.* 2005) is present in the crust. Taking the background resistivity of the respective layer into account, the resulting principle resistivities are $\varrho_{x1} = \varrho_{z1}$ = 1133.7 Ωm and $\varrho_{y1} = 4538.0$ Ωm for the upper crustal layer and $\varrho_{x2} = \varrho_{z2} = 113.8$ Ωm and $\varrho_{y2} = 3747.8$ Ωm for the lower crustal layer. The width of the anisotropic block was varied from 5, 10, 20, 50, 100, 150 and 200 km to infinite (i.e. the whole width of the numerical mesh). The anisotropy strike angle α_S was varied from 0° to 90° using 15° intervals. Note that anisotropy strike angles from 90° to 180° cause identical effects as the angles in the first quadrant, with 90° being the symmetry axis (i.e. the result of $\alpha_S = 15°$ is identical to that of $\alpha_S = 165°$, etc.). In 2-D, the anisotropy strike angle is defined as the angle between the regional strike direction (i.e. perpendicular to the profile direction) and the anisotropy strike direction. As the background model is 1-D, a pseudo-regional strike direction (i.e. North) perpendicular to the profile direction is assumed as reference for the anisotropy strike angle. As Brasse *et al.* (2009) state, the anisotropic dip (α_D) and slant (α_L) angles (if not too large) have much smaller influence on the transfer functions than the other parameters, so the influence on the inversion results is expected to be much smaller too. Therefore, to reduce complexity and the number of scenarios for this study the dip and slant angles were chosen to be $\alpha_D = \alpha_L = 0°$, which is also consistent with the dyke swarm scenario where 91% of the dykes are vertical and the other within 30° of vertical (Le Gall *et al.* 2005). Fig. 2(b) shows a general sketch representing the anisotropic models.

The 2-D anisotropy forward code by Pek & Verner (1997) was used to derive the synthetic responses for the various models. For numerical reasons, the anisotropic block is not outcropping; the top of it is 25 m below surface. The responses were calculated at 45 periods (from 0.04 to 1 000 s) at 49 locations with a 2.5 km site spacing centred over the lateral extent of the anisotropic block. These
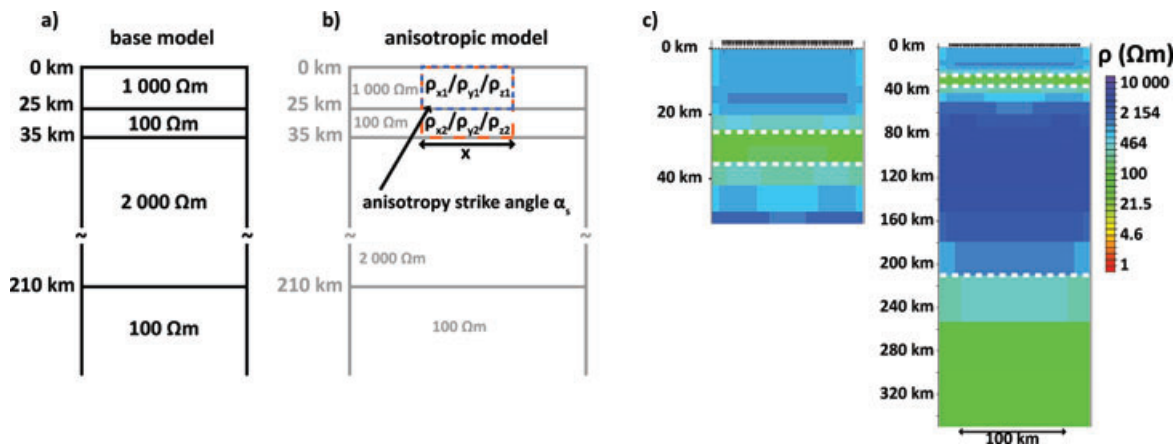
Figure 2. Sketches of the models to generate the synthetic data sets. The base model (a) is a simple layered model used as background model for the anisotropic models (b), which include an anisotropic block either in the top layer only (blue dashed line) or in both crustal layers (red dashed line). The lateral extent (x) of the block varies from 5 km to infinite (i.e. whole model width) and the anisotropy strike angle varies from 0° to 90°. The approximated principle resistivities are: $\varrho_{x1} = \varrho_{z1} = 1133.7\,\Omega$m, $\varrho_{y1} = 4538.0\,\Omega$m and $\varrho_{x2} = \varrho_{z2} = 113.8\,\Omega$m, $\varrho_{y2} = 3747.8\,\Omega$m. As reference the isotropic inversion result of the base model is shown in (c), where the white dashed lines represent the depths of the layer interfaces in the true model [vertical exaggeration = 3 for crustal scale (left) and 1 for lithospheric scale model (right)].

synthetic data were treated in the same manner as real data; namely, the strike angle analysis and decomposition code *strike* by McNeice & Jones (2001) was applied. The regional strike direction was fixed to North (i.e. perpendicular to the profile direction) to investigate the effects of the various anisotropy strike directions with respect to the regional strike direction. Enforcing the regional strike direction is required, because the presence of the anisotropic block affects the strike analysis and decomposition. A very simple two quarterspaces model (100 Ωm on the left and 1 000 Ωm to the right) shown in Fig. 3 illustrates the influence of an anisotropic block on the results of *strike*. Fig. 3(a) shows the obtained regional strike directions (red lines, subject to 90° ambiguity), twist angles (black values) and shear angles (blue values). A single-site, multi-frequency approach was applied to three different frequency bands (all frequencies, frequencies of the depths ranges 5–40 km and 50–150 km respectively). As expected, twist and shear angles are zero and the regional strike direction found is parallel to the contact surface of the two quarterspaces. A 45 -km-thick anisotropic layer was added in the models below (Fig. 3b–d). The anisotropic strike angle was 45° and the principle resistivities ($\varrho_x = \varrho_z = 550\,\Omega$m, $\varrho_y = 182\,\Omega$m) were calculated assuming anisotropy based on dykes of 100 Ωm (50%) and 1 000 Ωm (50%). The grey-shaded areas illustrate the anisotropic layer, which extends over the whole model (b), over the resistive quarterspace (c) and over the conductive quarterspace (d). Depending on the chosen data subset and model, the obtained regional strike direction can be very different from the true regional strike direction. In areas where the twist and shear angles are close to zero [e.g. resistive quarterspace in model (d)], the regional strike direction is recovered correctly. The converse argument that large twist and shear angles are related to incorrect regional strike directions is not valid. Note, that the regional strike directions and decomposition parameters represent the most ideal model (smallest average RMS value) for the chosen data subset, but a wide range of other regional strike directions can also be fit by distortion models with acceptable RMS values.

2.2 Isotropic inversions

The various sets of synthetic anisotropic data have been inverted isotropically using the 2-D finite difference, smooth model inver-

sion code within the WinGLink® software package by Geosystem developed by Rodi & Mackie (2001) [or rather using its improved version (Mackie 2002; Baba *et al.* 2006) applying isotropic settings]. Obtaining the final inversion model is an iterative process of re-running the inversion several times introducing more and more data. Therefore, the initial error floors were set to 2.5% for TM phase (equivalent to 0.7°), 25% for TE phase (7.0°) and 50% for the resistivities of both modes for the initial inversion run. Successively, the error floors of the TE phase of the TM resistivity and finally of the TE resistivity were reduced. The error floors of the final inversion run were 2.5% for phases and 5% for apparent resistivity values. To demonstrate that any artefacts in the final inversion model are caused by the anisotropic block, Fig. 2(c) shows the inversion result of the base model data. It is obvious that the layered background without any anisotropy effects is recovered well.

Fig. 4 shows the isotropic inversion results of models with a 50-km wide (indicated by red arrows), anisotropic block in the upper crustal layer (blue dashed line in Fig. 2b) for anisotropy strike directions from 0° to 90°. Although the top 25 km are clearly affected by the presence of the anisotropic block, the base of the lithospheric mantle, at about 210 km, is virtually unaffected and the lower crustal conductor only shows artefacts for anisotropy strike angles greater than 45°. If, on the other hand, the anisotropic block extends over both crustal layers (red dashed line in Fig. 2b), the effects on the inversion results are far more significant (Fig. 5). Again the upper crustal layer is strongly affected by the anisotropy. In this case the conductive lower crustal layer is also affected for all anisotropy strike directions, but a downward bent conductor is not present for small angles. Additionally, it becomes obvious that the depth to the lithosphere-asthenosphere boundary (LAB) can be significantly overestimated, especially for anisotropy strike directions from 15° to 45°. For these angles, the lithospheric mantle will also be inferred as more resistive than it actually is. Fig. 6 shows the influence of the width of an anisotropic block—in this case for an anisotropic block in both crustal layers and an anisotropy strike direction of 75°. It illustrates clearly that—as expected—the wider the anisotropic block the stronger the effects. Although for widths of 5 and 10 km hardly any effects are apparent, the downward bending of the lower crustal conductor, enhancement of the resistivity of the
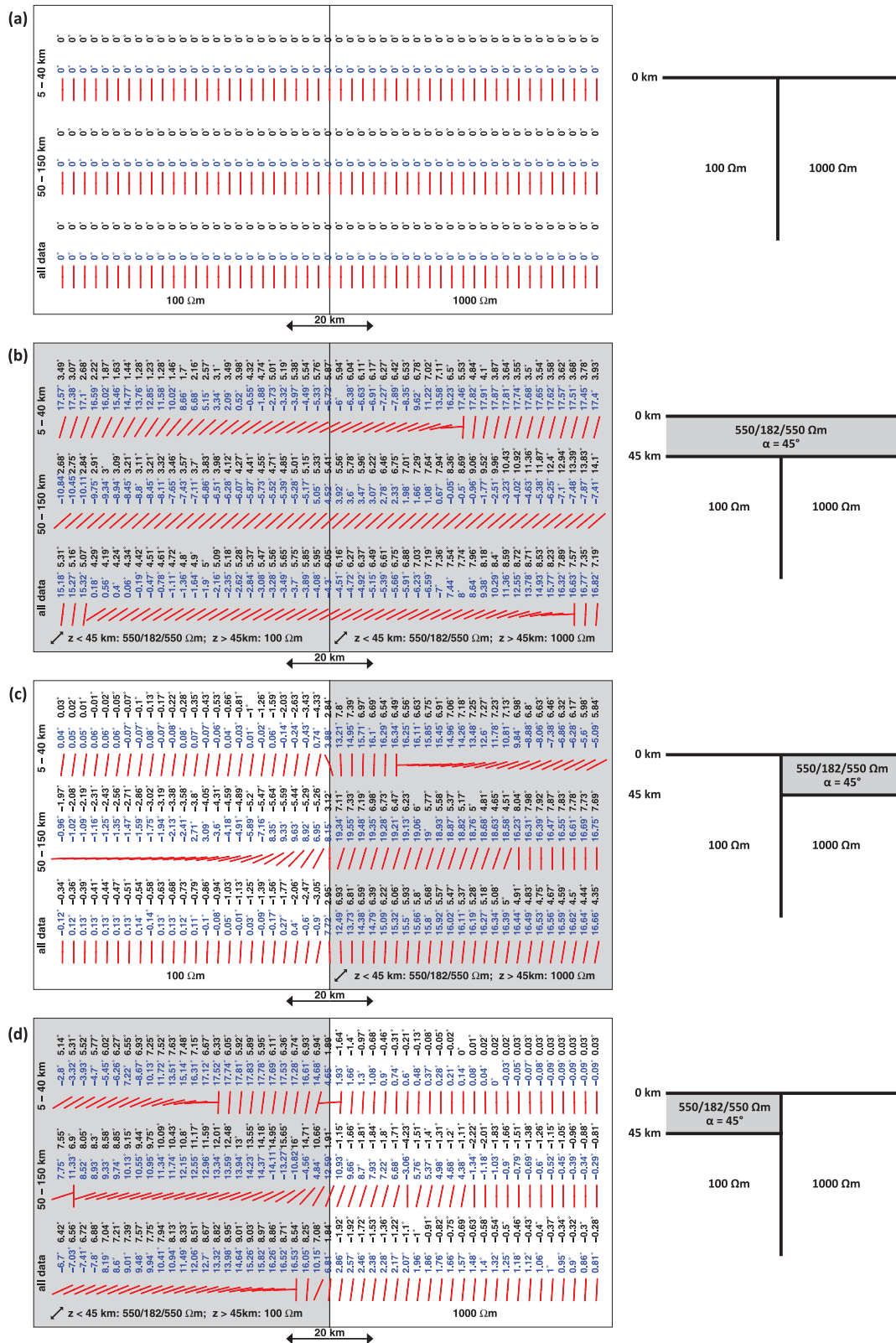
Figure 3. Strike analysis and decomposition results of a simple two quarterspace model (100 and 1 000 Ωm, respectively) with and without anisotropy. The left column shows the strike analysis and decomposition results along a profile crossing the fault (2.5 km site spacing) and at the right are sketches of the section view. Grey-shaded areas are anisotropic with principle resistivities $\varrho_x = \varrho_z = 550$ Ωm, $\varrho_y = 182$ Ωm and anisotropy strike angle 45°. Strike analysis and decomposition was performed in single-site, multifrequency mode using three different frequency bands (all frequencies, frequencies of 5–40 km and 50–150 km depths, respectively). The red lines represent the determined regional strike direction at each site (subject to 90° ambiguity), additional the obtained twist (black) and shear (blue) angles are stated. As reference, (a) shows the results obtained for an isotropic quarterspace model. In the models below an anisotropic layer of 45 km thickness was added cross the whole model (b), the resistive quarterspace (c) and the conductive quarterspace (d).
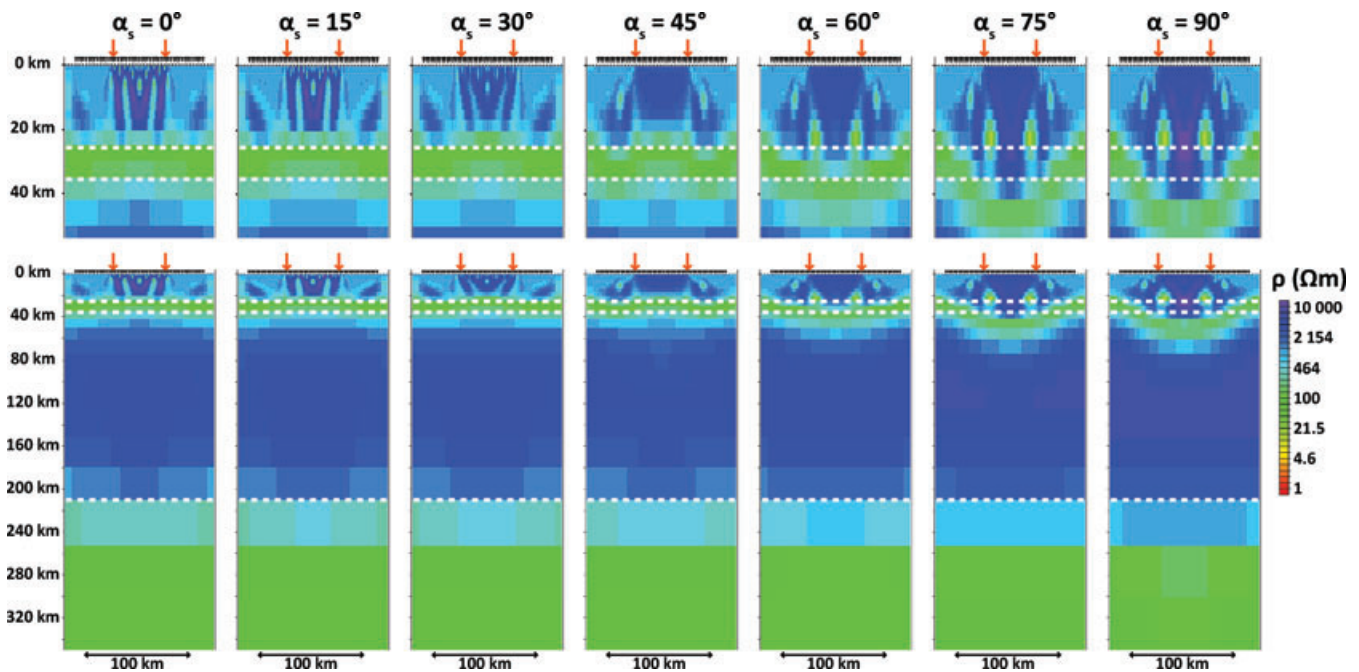
Figure 4. Isotropic inversion results of the data sets obtained from the models with a 50-km-wide anisotropic block in the top layer but different anisotropy strike angles (left to right: 0° to 90°). The red arrows indicate the lateral extent of the anisotropic block and the white dashed lines represent the depths of the layer interfaces in the true model (Fig. 2). At the bottom the sections are plotted with vertical exaggeration = 1, whereas on the top vertical exaggeration = 3 is used to make the near surface structures visible.
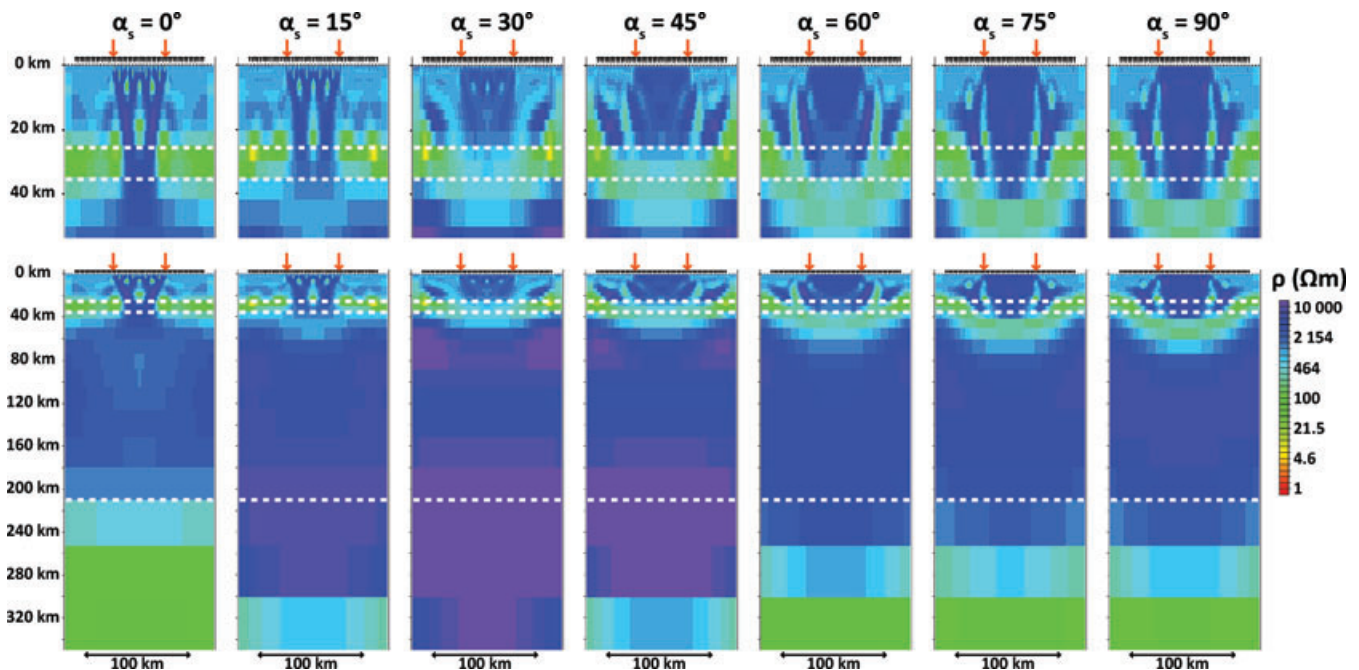

Figure 5. Isotropic inversion results of the data sets obtained from the models with a 50-km-wide anisotropic block in both crustal layers but different anisotropy strike angles (left to right: 0–90°). The red arrows indicate the lateral extent of the anisotropic block and the white dashed lines represent the depths of the layer interfaces in the true model (Fig. 2). At the bottom, the sections are plotted with vertical exaggeration = 1, whereas on the top vertical exaggeration = 3 is used to make the near surface structures visible.

lithospheric mantle and the increasing depth of the LAB becomes more and more significant with increasing width of the anisotropic block.

Fig. 7 shows resistivity-depth profiles of these synthetic tests. The coloured lines represent the different anisotropy strike directions for the scenarios of a 50-km-wide anisotropic block in the upper crustal layer (left) and in both crustal layers (middle), and the dashed black line shows the base model resistivity-depth profile. For the anisotropic block in both crustal layers with anisotropic strike direction 75° the different widths (right) are represented by coloured lines (base model as black dashed line for comparison). The resistivity-depth profiles illustrate that for the scenario with
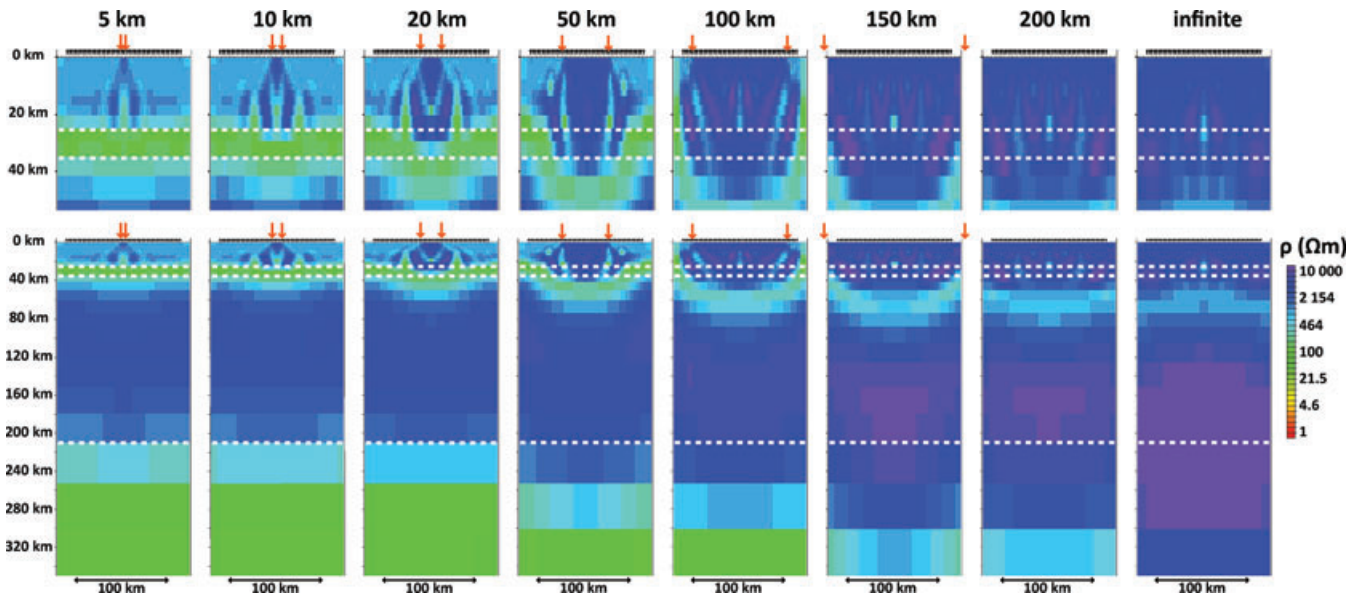
Figure 6. Isotropic inversion results of the data sets obtained from the models with an anisotropic block in both crustal layers and an anisotropy strike angle of 75° but varying lateral extent of the anisotropic block (left to right: 5 km to infinite, i.e. whole model width). The red arrows indicate the lateral extent of the anisotropic block and the white dashed lines represent the depths of the layer interfaces in the true model (Fig. 2). At the bottom the sections are plotted with vertical exaggeration = 1, whereas on the top vertical exaggeration = 3 is used to make the near surface structures visible.
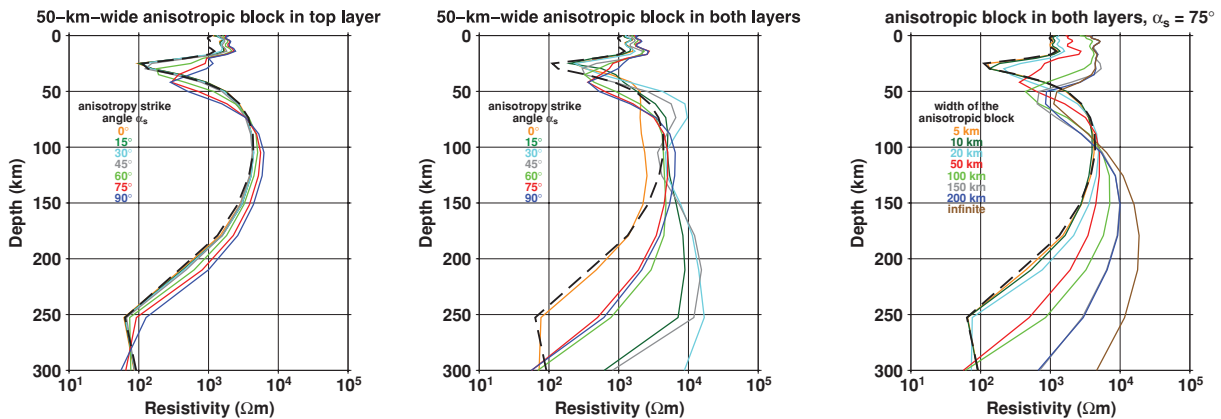

Figure 7. Average resistivity-depth profiles presenting the inversions results shown in Figs 4, 5 and 6. The average resistivity values (calculated as the mean of the log arithmetic resistivity values) were estimated over the width of the anisotropic block (or maximum over the part covered by sites). Profiles are shown for a 50-km-wide anisotropic block of different anisotropy strike direction in the upper crustal layer (left) and in both layers (middle) as well as for an anisotropic block in both crustal layers with $\alpha_S = 75°$ but varying width. The black dashed line represents the resistivity-depth profile of the base model.

anisotropy in the upper crustal layer the lithospheric mantle remains basically unaffected and only large anisotropy strike directions show a downward shift of the crustal conductor. For the scenario with the anisotropic block in both crustal layers it is obvious that the anisotropic strike directions from 15° to 45° have the strongest effect on the lithosphere, whereas large obliquity angles (60°, 75° and 90°) cause the larger downward shift of the crustal conductor and an approximate 40 km thicker lithospheric mantle; the profile of $\alpha_S = 0°$ is the least affected. Considering the resistivity-depth profiles of the varying width of the anisotropic block, it is clear that anisotropic blocks of small width (20 km and less) essentially do not cause any significant changes in the average resistivity. For widths of 50 km and more the increasing width goes along with enhancement in the effects on the resistivity-depth profile (i.e. downward shift of the crustal conductor and the LAB as well as overestimation of the lithospheric mantle resistivity). The resistivity-depth profiles

illustrate clearly, but in a different manner, and emphasize what was found for the inversion models in Figs 4–6.

In addition, slightly modified scenarios have also been tested:

(1) *Conductive cover layer*: A conductive (10 Ωm) layer of 2 and 5 km thickness, respectively, was introduced directly beneath the surface, whereas the rest of the model remained identical to the base model with a 50-km wide, anisotropic block in both crustal layers and an anisotropy strike direction of 75°. Fig. 8 shows, on the left half, the isotropic inversion results of these conductive cover layer cases. For both thicknesses two models are shown—on the left the model obtained for the isotropic base model including the cover layer is shown in comparison to the isotropic inversion result of the model with a 50-km wide, anisotropic block in both layers including the cover layer (on the right). It is apparent that a conductive cover layer reduces the misleading effects of the isotropic inversion of
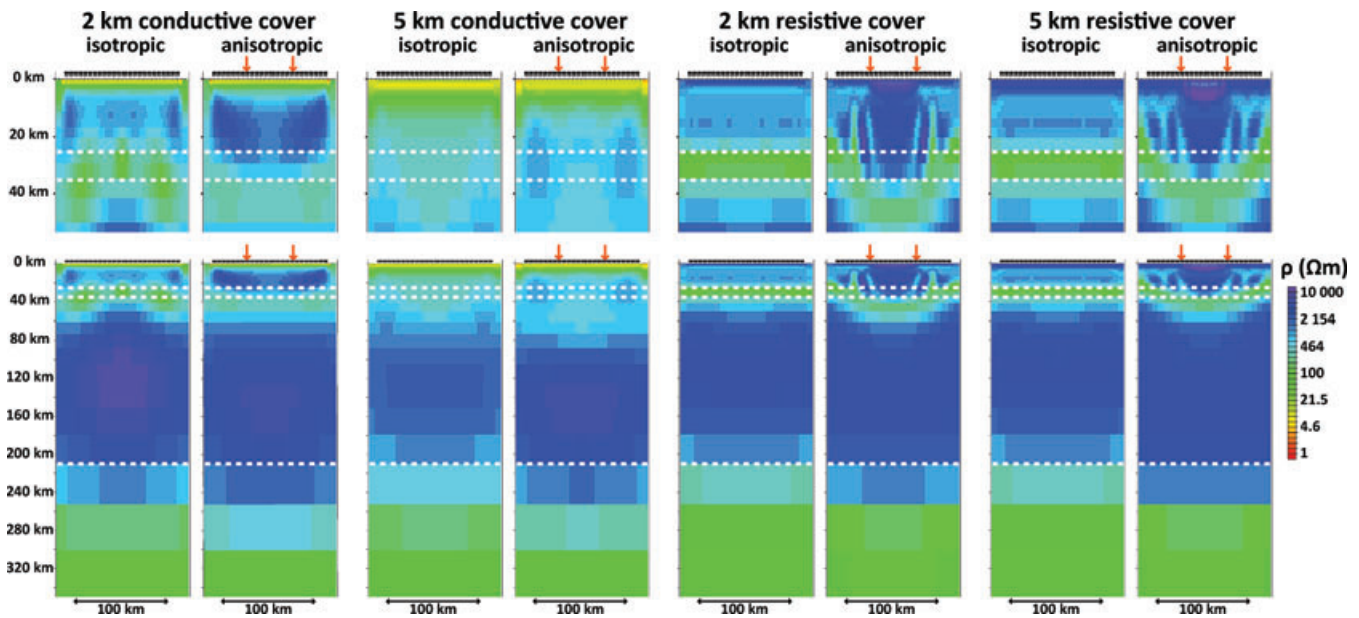
Figure 8. Inversion results of models with an additional cover layer. Both, conductive (10 Ωm) and resistive (5 000 Ωm), cover layers of 2 and 5 km thickness have been investigated. For each of these scenarios on the left the inversion result of the isotropic layered base model including cover layer is shown in comparison to the isotropic inversion result of the model with a 50-km-wide anisotropic block ($\alpha_S = 75°$) in both crustal layers including the cover layer on the right. The red arrows indicate the lateral extent of the anisotropic block and the white dashed lines represent the depths of the layer interfaces in the true model (Fig. 2). At the bottom, the sections are plotted with vertical exaggeration = 1, whereas on the top vertical exaggeration = 3 is used to make the near surface structures visible.

anisotropic structures. The 2-km-thick cover layer shows enhanced resistivities for the upper crustal layer and greater depths of the conductive, lower crustal layer and the LAB than found for the isotropic layered background model. In the case of the 5 km conductive cover, the upper crustal part is almost unaffected, but the resistivity is enhanced in the lower crust and slightly reduced in the upper lithospheric mantle. The LAB appears again at greater depth than in the base model. Nevertheless, the effects of isotropic inversion of anisotropic data are less extreme and bizarre than without a cover layer.

(2) *Resistive cover layer*: A resistive (5000 Ωm) layer of 2 and 5 km thickness, respectively, was introduced directly beneath the surface, whereas the rest of the model remained identical to the base model with a 50-km wide, anisotropic block in both crustal layers and an anisotropy strike direction of 75°. Fig. 8 shows, on the right half, the isotropic inversion results of these resistive cover layer cases. For both thicknesses two models are shown—on the left the model obtained for the isotropic base model including the cover layer is shown in comparison to the isotropic inversion result of the model with a 50-km wide, anisotropic block in both layers including the cover layer (on the right). For both cover layer thicknesses the depth of the LAB is slightly enhanced and the crustal layers are still strongly affected by the isotropic inversion of the anisotropic data set. Also the downward bent conductive, lower crustal layer remains present. It is obvious that a resistive cover layer reduces the effects much less than a conductive cover layer of the same thickness.

(3) *Larger site spacing*: Fig. 9 shows the inversion results for a 50-km-wide anisotropic block both in the upper crustal and in both crustal layers for an anisotropy strike direction of 0° and 75°, respectively, obtained using a 10 km rather than a 2.5 km (compare Figs 4 and 5) site spacing. None of these four scenarios shows major differences between the 2.5 and 10 km site spacing inversion results. Therefore, we can reject the hypothesis that the observed effects are related to the site spacing chosen.

2.3 Anisotropic inversions

For anisotropic inversions, the program by Mackie (2002) and Baba *et al.* (2006) was applied to the synthetic test data sets. It is a finite-difference code that finds the regularised solutions (Tikhonov Regularisation) to the 2-D inverse problem using the method of non-linear conjugate gradients (Mackie 2002). Beside the common regularization and weighting function parameters to trade-off data misfit and model structure (in general and/or horizontal and vertical directions separately) this program uses an additional isotropy regularisation parameter τ_{iso}. As the algorithm solves for three resistivity models ϱ_{xx}, ϱ_{yy} and ϱ_{zz} (i.e. one model each for the main diagonal elements of the diagonalized anisotropic resistivity matrix), the isotropy regularisation parameter is the weighting of the constraint that tries to keep the three models as similar as possible, that is the result as isotropic as possible. Higher values of τ_{iso} will result in more isotropic models, whereas lower values allow for a larger variation between the models of the three different directions. To enforce an isotropic model, $\tau_{iso} = 100$ or higher should be selected, whereas $\tau_{iso} = 0$ gives the program the complete freedom to make the model as anisotropic as possible (Mackie 2002). Note that this program is a restricted one and is based on the assumption that the anisotropy is aligned with the coordinate system axes (i.e. parallel to the inversion mesh edges). Therefore, the anisotropy strike, slant and dip angles are all assumed to be zero. Thus, a $\tau_{iso} = 0$ means that the TE and TM data are fit independently.

Fig. 10 shows anisotropic inversion results for different isotropy regularization parameters $\tau_{iso} = 10$, 1 and 0 and isotropic inversion results of the individual modes (TE mode data only and TM mode data only, respectively). The data set inverted is that of the 50-km wide, anisotropic block in both crustal layers with a direction of $\alpha_S = 0°$. This angle conforms with the assumption the inversion code is based on; namely, anisotropy being aligned with the coordinate system. Note, as most of the current flow in the MT problem is
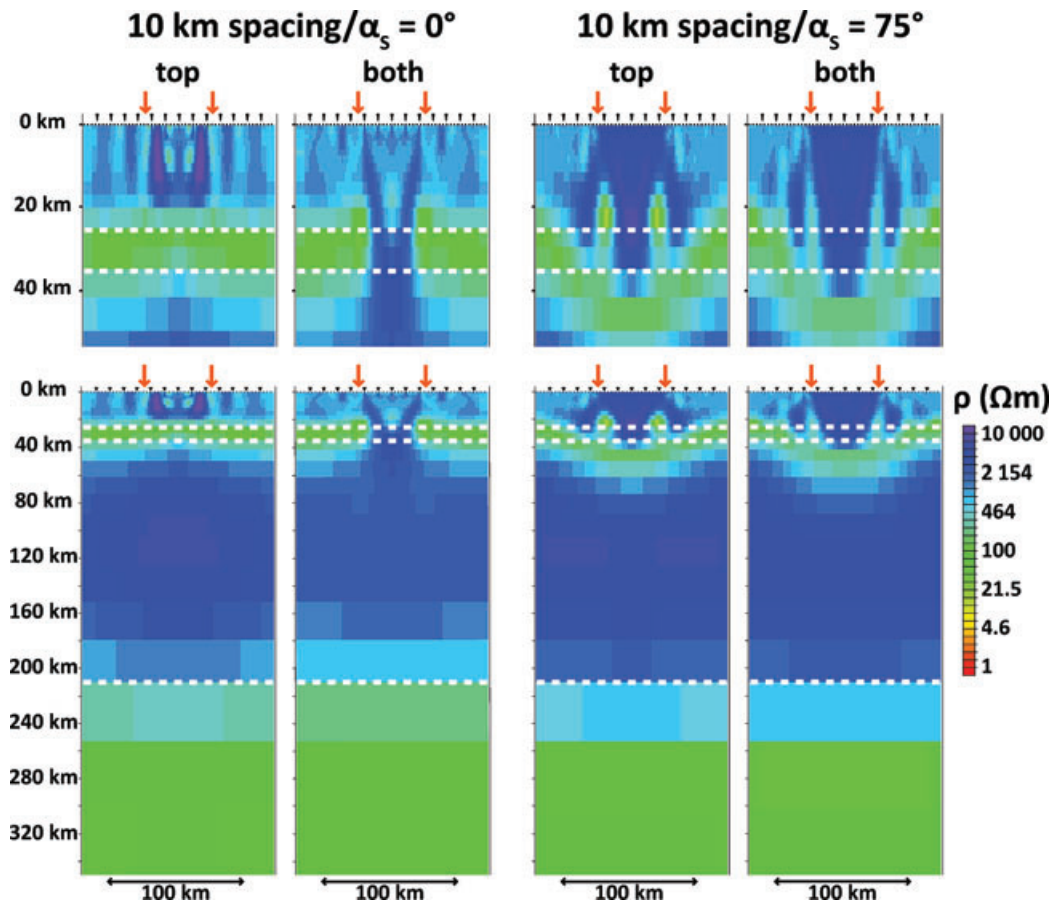
Figure 9. Inversion results of models with increased site spacing. Isotropic inversion result of the model with a 50-km-wide, anisotropic block in either the upper crustal or both crustal layers with either $\alpha_S = 0°$ or $\alpha_S = 75°$ have been recalculated using a 10 km site spacing (rather than 2.5 km; compare Figs 4 and 5). The red arrows indicate the lateral extent of the anisotropic block and the white dashed lines represent the depths of the layer interfaces in the true model (Fig. 2). At the bottom the sections are plotted with vertical exaggeration = 1, whereas on the top vertical exaggeration = 3 is used to make the near surface structures visible.
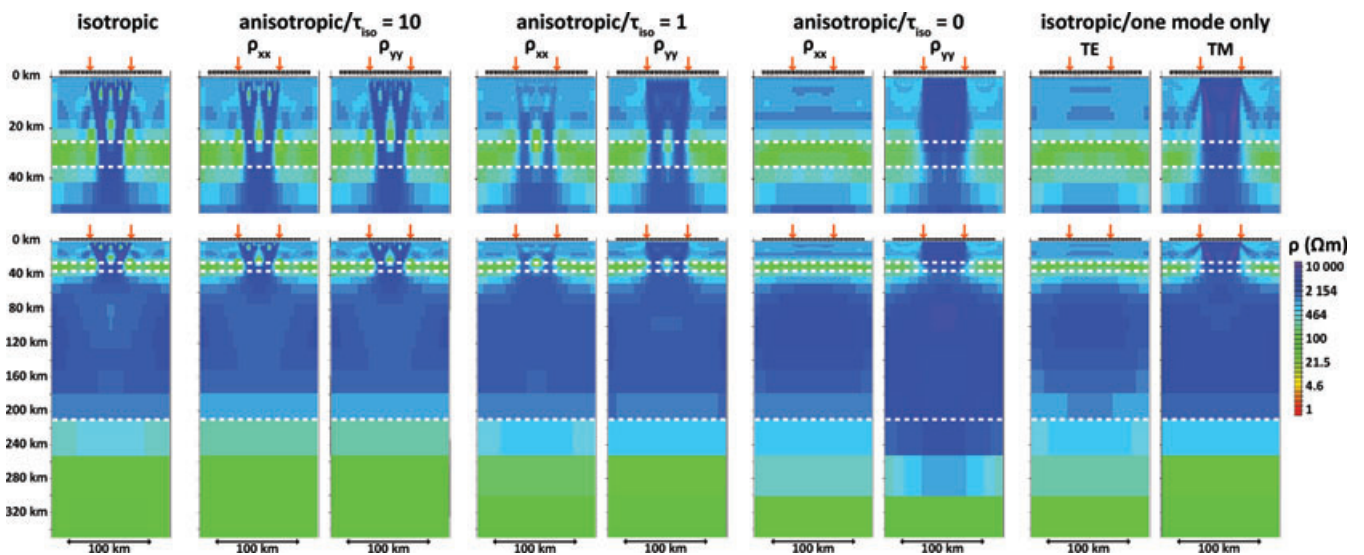

Figure 10. Anisotropic inversion results of the data sets obtained from the model with a 50-km-wide, anisotropic block in both crustal layers and an anisotropy strike angle of 0°. The isotropic inversion result (taken from Fig. 5) is shown in comparison to the anisotropy inversion models, which have been obtained using different isotropy regularization parameters $\tau_{iso} = 10$, 1 and 0. The models of the two horizontal resistivity components (ϱ_{xx} and ϱ_{yy}) are shown in comparison to the results of TE-mode-only and TM-mode-only isotropic inversion (on the right). The red arrows indicate the lateral extent of the anisotropic block and the white dashed lines represent the depths of the layer interfaces in the true model (Fig. 2). At the bottom the sections are plotted with vertical exaggeration = 1, whereas on the top vertical exaggeration = 3 is used to make the near surface structures visible.
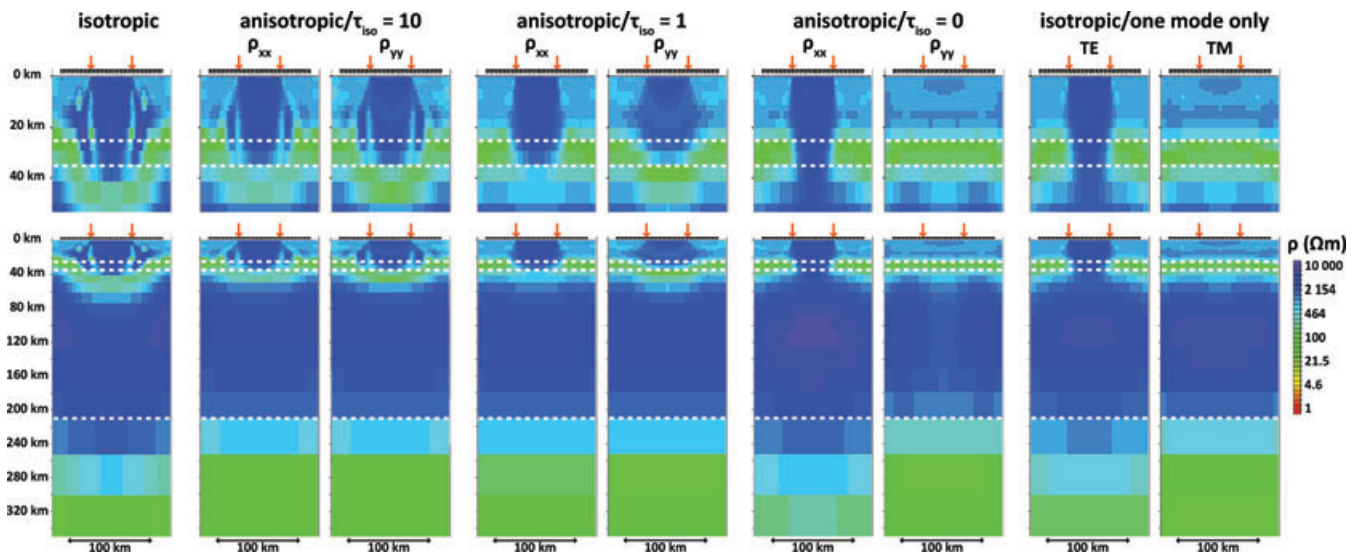
Figure 11. Anisotropic inversion results of the data sets obtained from the model with a 50-km wide, anisotropic block in both crustal layers and an anisotropy strike angle of 75°. The isotropic inversion result (taken from Fig. 5) is shown in comparison to the anisotropy inversion models, which have been obtained using different isotropy regularization parameters τ_{iso} = 10, 1 and 0. The models of the two horizontal resistivity components (ϱ_{xx} and ϱ_{yy}) are shown in comparison to the results of TE-mode-only and TM-mode-only isotropic inversion (on the right). The red arrows indicate the lateral extent of the anisotropic block and the white dashed lines represent the depths of the layer interfaces in the true model (Fig. 2). At the bottom the sections are plotted with vertical exaggeration = 1, whereas on the top vertical exaggeration = 3 is used to make the near surface structures visible.

horizontal, it is particularly difficult to resolve the model of ϱ_{zz} (Mackie 2002). Therefore, the figure only shows the two models related to the horizontal components (ϱ_{xx} and ϱ_{yy}). For an isotropy regularisation parameter τ_{iso} = 10, the two models are basically identical and very similar to the isotropic inversion result (τ_{iso} = 10^6; shown in Fig. 5). Reducing the parameter to τ_{iso} = 1, the models show differences in the crustal parts. Although the upper crust for ϱ_{xx} becomes more homogeneous, the location of the dykes appear more as a solid block in the ϱ_{yy} model. The LAB depth appears slightly increased. Using τ_{iso} = 0, that is independent models for ϱ_{xx} and ϱ_{yy} (and also for ϱ_{zz}), the anisotropic structure in both crustal layers is well recovered, whereas the LAB depth is increased, especially for the ϱ_{yy} model. For comparison, the isotropic inversion results of the TE-mode-only and TM-mode-only data, respectively, are shown in Fig. 10. Although these models are not identical to the anisotropic inversion results using τ_{iso} = 0, they are (for such a simple model) very similar and represent the model reasonable well. Although the anisotropic models of τ_{iso} = 0 represent the crustal part in the presence of the anisotropic structure better, the isotropic one-mode-only results estimate the LAB depth more accurately.

Using the data set of the 50-km wide, anisotropic block in both layers with strike direction α_S = 75°, the performance of the anisotropic code applied to data sets failing the assumption of anisotropy parallel to the coordinate axes is tested. Fig. 11 shows the results of this test. Using τ_{iso} = 10 results in identical models for ϱ_{xx} and ϱ_{yy} that are similar to the isotropic inversion result. Reducing the value of τ_{iso} to 1 improves the resolution of the crustal structures, especially for the ϱ_{xx} model, where the lower crustal conductor is no longer downward bent into the lithospheric mantle. For both τ_{iso} = 10 and 1 the LAB depth is slightly increased. The independent inversion models (i.e. τ_{iso} = 0) represent the true model similarly as well as they do for the case with the anisotropy strike direction parallel to the axes (Fig. 10, considering that a change in the anisotropic strike direction of almost 90° results in the more conductive direction to be associated with the other mode, that is ϱ_{xx} corresponds to the TE mode and the TM mode respectively).

Again, the isotropic one-mode-only inversion results perform well and show very similar structures to the models for τ_{iso} = 0. The lower crustal conductor and the anisotropic block are recovered, only the LAB depth is overestimated in the ϱ_{xx} and TE-only models, respectively. Although the anisotropy strike direction was not aligned with the coordinate system, the anisotropic inversion, as well as the one-mode-only inversion, produced superior models to a standard isotropic inversion of both modes jointly.

3 CASE HISTORY

The regional strike direction found for the ZIM line is 35°E of N, whereas the direction of the dykes of the Okavango Dyke Swarm is 110° E of N. Thus, the anisotropy strike angle of the dykes with respect to the ZIM line and its regional strike direction can be translated to α_S = 75° (sketched in Fig. 12). Therefore, the settings are similar to those of the models shown for the 50-km-wide anisotropic block (width of the dyke swarm 50–60 km) with α_S = 75° in Figs 4 and 5 (and the anisotropic inversion shown in Fig. 11). Both synthetic models clearly show a downward bent conductive layer in the upper lithospheric mantle that is an artefact of the isotropic inversion. The synthetic test and the presence of a lower crustal conductor in neighbouring terranes strongly suggest that also in the real data case the downward bent conductor is not a real structure but an artefact. As the depth extent of the Okavango dykes is uncertain (4–30 km based on magnetic data estimates; Dailey *et al.* 2009), both scenarios, anisotropy in the upper crustal layer only and in both crustal layers, are possible. Therefore, it cannot be excluded that the LAB depth of 220 ± 20 km (Miensopust *et al.* 2011) is possibly overestimated by up to approximately 40 km.

Beneath the ZIM line the subsurface structure, besides the Okavango Dyke Swarm (introducing anisotropy), is more complex than the very simple 1-D layered background model used for the synthetic tests. Therefore, an anisotropic inversion was only performed for the sites located above the dyke swarm to reduce the complexity. Fig. 13 shows the model of an isotropic inversion of
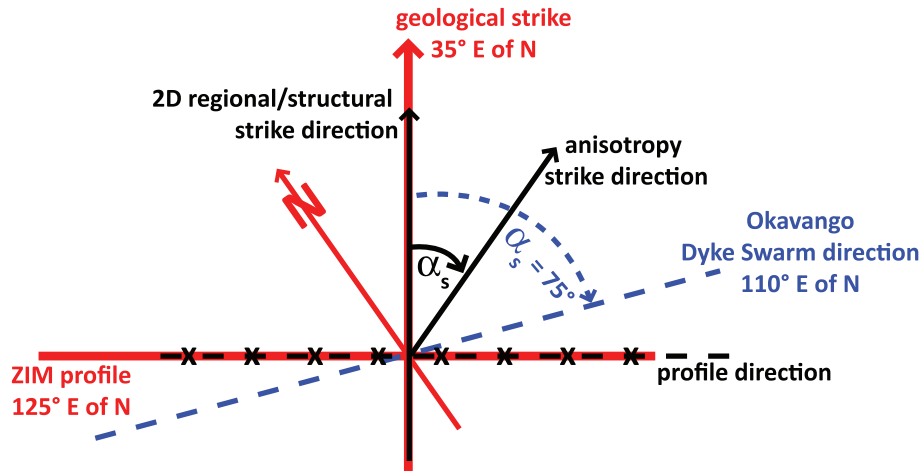
Figure 12. Sketch to illustrate the relation between the ZIM line case study and the anisotropy strike direction of the synthetic tests. The ZIM line profile direction and the geological strike direction with respect to true north are shown in red. The profile direction and regional strike direction as used by the synthetic 2-D anisotropy models are overlain in black illustrating that the angle between regional and anisotropy strike direction is given by the anisotropy strike angle α_S. In addition, the 110°E of N orientated Okavango Dyke Swarm is shown in blue and its direction is translated into an anisotropy strike angle $\alpha_S = 75°$ with respect to the ZIM line regional strike direction.
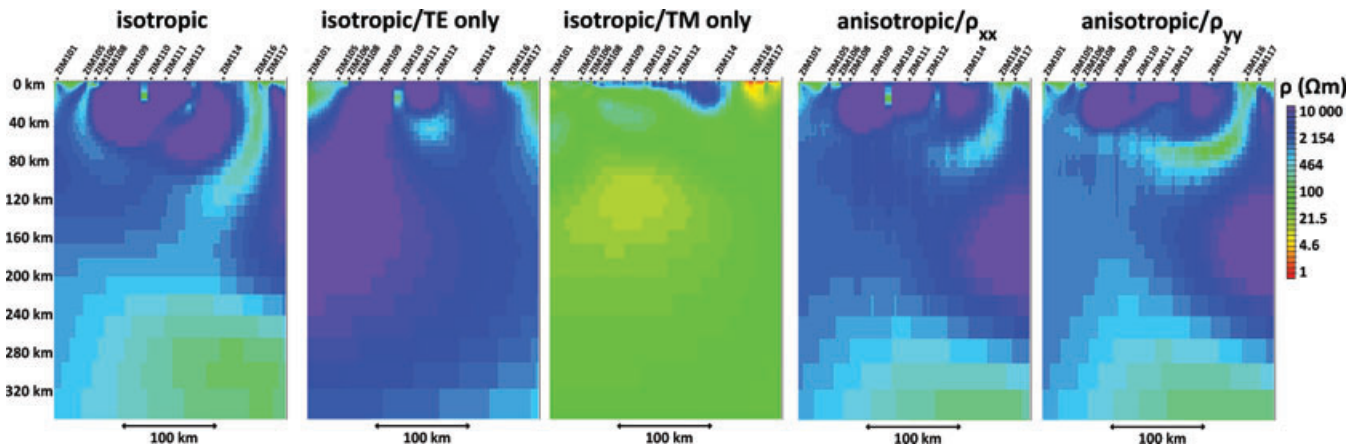

Figure 13. Inversion results of the Okavango Dyke Swarm part of the ZIM line. Isotropic inversion of TE and TM mode, the TE mode only and the TM mode only, respectively, are shown on the left to middle. Anisotropic inversion results (using $\tau_{iso} = 1$) represented by the models of the two horizontal resistivity components (ϱ_{xx} and ϱ_{yy}) are shown on the right.

this data subset for comparison (left), the models of TE mode only and TM mode only isotropic inversions (middle) and the models of the two horizontal resistivity components (ϱ_{xx} and ϱ_{yy}) obtained from anisotropic inversion using an isotropy regularisation parameter $\tau_{iso} = 1$ (right). (For $\tau_{iso} = 0$ the models look very similar to the one-mode-only isotropic models.) The results of the one-mode-only inversion are considered unrealistic. Nevertheless, the TE mode model, showing the strong resistor, whereas the TM mode model is basically unaffected, is similar to the results found for the synthetic test with the 75° anisotropy strike direction (Fig. 11) and, therefore, is consistent with the dyke swarm orientation. The results of the anisotropic inversion ($\tau_{iso} = 1$) show a strong resistor in both models (ϱ_{xx} and ϱ_{yy}), but the vertical extent is limited to the crust (upper 35–40 km; compare with isotropic inversion (left) and Fig. 1, where it extends to 60–80 km depth). There is no clear lower-crust conductor recognisable as seen in the synthetic tests, but compared to the isotropic inversion result (left and Fig. 1) the top of the less resistive zone is now located at about 40 km depth

rather than 60–80 km. The LAB appears at a similar depth as for the original isotropic inversion. Although the true subsurface structure is probably not presented correctly by any of these models, it nevertheless is apparent that the strong resistor is a crustal structure that is related to the Okavango Dyke Swarm. Obvious also is that this structure is anisotropic on the MT scale and affects the isotropic model. Therefore, the downward bent conductor is believed to be such an artefact. Unfortunately, the true LAB depth remains somewhat uncertain; one can exclude that its depth is underestimated but it might be overestimated by 20–40 km.

4 CONCLUSIONS

The nature of anisotropy and effects when undertaking isotropic inversions have been examined. The complexity and variety of possible synthetic models is unlimited, and only a few very specific and simple models have been shown here, nevertheless these tests illustrated the influence on strike analysis and decomposition and made

obvious how different the effects of isotropic inversion applied to data from an anisotropy Earth can be. The tests show for a simple layered background model that resistivity values can be overestimated, that horizontal conductive layers can appear downward bent, and depths of layer interfaces might not be correctly located. One cannot be certain about the resistivity distribution obtained from isotropic inversion if anisotropy is present, as the effects can vary from negligible to highly significant. Therefore, extensive testing of synthetic model scenarios, one-mode-only and anisotropic inversion approaches is strongly recommended, if there is the suspicion of anisotropic resistivity structures being present.

The synthetic tests with scenarios modelled based on the case history of the ZIM profile (affected by the Okavango Dyke Swarm) showed that the unusual conductor in the lithospheric mantle is an artefact and is likely located in the lower crust, as for the neighbouring terranes. Additionally, the possible overestimation of the LAB depth under these conditions could be occurring by up to about 40 km, if the dykes extend as deep as into the lower crustal conductor. The focussed, anisotropic inversion of the dyke swarm area shows the resistor associated with the dyke swarm as a crustal structure. The complexity of the subsurface structure, compared to the simple layered 1-D background model of the synthetic tests, causes less ideal anisotropic inversion results. Nevertheless, they support some of the assumptions made (e.g. the dyke swarm is a resistive crustal structure that affects the isotropic model). Unfortunately, the anisotropic models are not able to localize the LAB depth any more accurately, that is the best estimate remains to be 220 ± 20 km with a possible overestimation of up to 40 km.

ACKNOWLEDGMENTS

REFERENCES

Aubourg, C., Tshoso, G., le Gall, B., Bertrand, H., Tiercelin, J.-J., Kampunzu, A.B., Dyment, J. & Modisi, M., 2008. Magma flow revealed by magnetic fabric in the Okavango giant dyke swarm, Karoo igneous province, northern Botswana, *J. Volc. Geotherm. Res.,* **170,** 247–261.

Baba, K., Chave, A.D., Evans, R.L., Hirth, G. & Mackie, R.L., 2006. Mantle dynamics beneath the East Pacific Rise at 17° S: insights from the Mantle Electromagnetic and Tomography (MELT) experiment, *J. geophys. Res.,* **111,** B02101, doi:10.1029/2004JB003598.

Bahr, K. & Simpson, F., 2002. Electrical anisotropy below slow- and fast-moving plates: paleoflow in the upper mantle?, *Science,* **295,** 1270–1272.

Bailey, R.C. & Groom, R.W., 1987. Decomposition of the magnetotelluric impedance tensor which is useful in the presence of channelling, in *Expanded Abstracts of the 57th Annual International Society of Exploration Geophysicists Meeting and Exposition*, Tulsa, OK, Vol. **57,** pp. 154–156.

Brasse, H., Kapinos, G., Li, Y., Mtschard, L., Soyer, W. & Eydam, D., 2009. Structural electrical anisotropy in the crust at the South-Central Chilean continental margin as inferred from geomagnetic transfer functions, *Phys. Earth planet. Inter.,* **173,** 7–16, doi: 10.1016/j.pepi.2008.10.017.

Caldwell, T.G., Bibby, H.M. & Brown, C., 2004. The magnetotelluric phase tensor, *Geophys. J. Int.,* **158,** 457–469.

Caricchi, L., Gaillard, F., Mecklenburgh, J. & Trong, E.L., 2011. Experimental determination of electrical conductivity during deformation of

melt-bearing olivine aggregates: implications for electrical anisotropy in the oceanic low velocity zone, *Earth planet. Sci. Lett.,* **302,** 81–94.

Dailey, M.K.M., Mortimer, D.J. & Atekwana, E.A., 2009. Using 2d and 3d modelling to infer the depth of the Okavango Dyke Swarm, AGU Fall Meeting, San Francisco, USA.

Davey, F.J. *et al.*, 1998. Preliminary results from a geophysical study across a modern, continent-continent collisional plate boundary—the Southern Alps, New Zealand, *Tectonophysics,* **288,** 221–235.

Eaton, D.W., Jones, A.G. & Ferguson, I.J., 2004. Lithospheric anisotropy structure inferred from collocated teleseismic and magnetotelluric observations: Great Slave Lake shear zone, northern Canada, *Geophys. Res. Lett.,* **31**(19), L19614, doi: 10.1029/2004GL020939.

Eisel, M. & Bahr, K., 1993. Electrical anisotropy in the lower crust of—an interpretation of a magnetotelluric profile after tensor decomposition, *J. Geomag. Geoelectr.,* **45,** 1115–1126.

Eisel, M. & Haak, V., 1999. Macro-anisotropy of the electrical conductivity of the crust: a magnetotelluric study of the German Continental Deep drilling site (KTB), *Geophys. J. Int.,* **136,** 109–122.

Elburg, M. & Goldberg, A., 2000. Age and geochemistry of Karoo dolerite dykes from northeast Botswana, *J. Afr. Earth Sci.,* **31,** 539–554.

Gatzemeier, A. & Moorkamp, M., 2005. 3d modelling of electrical anisotropy from electromagnetic array data: hypothesis testing for different upper mantle conduction mechanisms, *Phys. Earth planet. Inter.,* **149,** 225–242.

Groom, R.W. & Bailey, R.C., 1989. Decomposition of magnetotelluric impedance tensors in the presence of local three-dimensional galvanic distortion, *J. geophys. Res. (Solid Earth),* **94**(B2), 1913–1925.

Hamilton, M.P. *et al.*, 2006. Electrical anisotropy of South African lithosphere compared with seismic anisotropy from shear-wave splitting analysis, *Phys. Earth planet. Inter.,* **158,** 226–239.

Heise, W. & Pous, J., 2003. Anomalous phases exceeding 90° in magnetotellurics: anisotropic model studies and a field example, *Geophys. J. Int.,* **155**(1), 308–318.

Heise, W., Caldwell, T.G., Bibby, H.M. & Brown, C., 2006. Anisotropy and phase splits in magnetotellurics, *Phys. Earth planet. Inter.,* **158,** 107–121.

Jourdan, F., Féraud, G., Bertrand, H., Kampunzu, A.B., Tshoso, G., Le Gall, B., Tiercelin, J.J. & Capiez, P., 2004. The Karoo triple junction questioned: evidence from Jurassic and Proterozoic $^{40}Ar/^{39}Ar$ ages and geochemistry of the giant Okavango dyke swarm (Botswana), *Earth planet. Sci. Lett.,* **222,** 989–1006.

Jourdan, F., Féraud, G., Bertrand, H., Watkeys, M.K., Kampunzu, A.B. & LeGall, B., 2006. Basement control on dyke distribution in Large Igneous Provinces: case study of the Karoo triple junction, *Earth planet. Sci. Lett.,* **241,** 307–322.

Kellett, R.L., Mareschal, M. & Senechal, G., 1992. A model of lower crustal electrical anisotropy for the Pontiac sub-province of the Canadian shield, *Geophys. J. Int.,* **111,** 141–150.

Kurtz, R.D., Craven, J.A., Niblett, E.R. & Stevens, R.A., 1993. The conductivity of the crust and mantle beneath the Kapuskasing Uplift: electrical anisotropy in the upper mantle, *Geophys. J. Int.,* **113,** 483–498.

Le Gall, B. *et al.*, 2002. $^{40}Ar/^{39}Ar$ geochronology and structural data from the giant Okavango and related dyke swarms, Karoo igneous province, Botswana, *Earth planet. Sci. Lett.,* **202,** 595–606.

Le Gall, B. *et al.*, 2005. The Okavango giant mafic dyke swarm (NE Botswana): its structural significance within the Karoo Large Igneous Province, *J. Struct. Geol.,* **27,** 2234–2255.

Leibecker, J., Gatzemeier, A., Hönig, M., Kuras, O. & Soyer, W., 2002. Evidences of electrical anisotropic structures in the lower crust and the upper mantle beneath the Rhenish Shield, *Earth planet. Sci. Lett.,* **202,** 289–302.

Mackie, R.L., 2002. User Manual and Software Documentation for Two-Dimensional Inversion of Magnetotelluric data. Anisotropy Version 6.7, GSY-USA, Inc., San Francisco, CA, USA.

Mareschal, M., Kellett, R.L., Kurtz, R.D., Ludden, J.N., Ji, S. & Bailey, R.C., 1995. Archean cratonic roots, mantle shear zones and deep electrical anisotropy, *Nature,* **375,** 134–137.

McNeice, G.W. & Jones, A.G., 2001. Multisite, multifrequency tensor decomposition of magnetotelluric data, *Geophysics,* **66**(1), 158–173.

Miensopust, M.P., 2010. Multidimensional Magnetotellurics: A 2D case study and a 3D approach to simultaneously invert for resistivity structure and distortion parameters, *PhD thesis*, Faculty of Science, Department of Earth and Ocean Sciences, National University of Ireland, Galway, Ireland.

Miensopust, M.P., Jones, A.G., Muller, M.R., Garcia, X. & Evans, R.L., 2011. Lithospheric structures and Precambrian terrane boundaries in northeastern Botswana revealed through magnetotelluric profiling as part of the Southern African Magnetotelluric Experiment, *J. geophys. Res.,* **116,** B02401, doi: 10.1029/2010JB007740.

Muller, M.R. *et al.*, 2009. Lithospheric structure, evolution and diamond prospectivity of the Rehoboth Terrane and the western Kaapvaal Craton, southern Africa: constraints from broadband magnetotellurics, *Lithos,* **112S,** 93–105, doi: 10.1016/j.lithos.2009.06.023.

Padilha, A.L., Vitorello, I., Padua, M.B. & Bologna, M.S., 2006. Lithospheric and sublithospheric anisotropy beneath central-southeastern Brazil constrained by long period magnetotelluric data, *Phys. Earth planet. Inter.,* **158**(2–4), 190–209.

Pek, J. & Santos, F. A.M., 2002. Magnetotelluric impedances and parametric sensitivities for 1-D anisotropic layered media, *Comput. Geosci.,* **28,** 939–950.

Pek, J. & Verner, T., 1997. Finite-difference modelling of magnetotelluric fields in two-dimensional anisotropic media, *Geophys. J. Int.,* **128,** 505–521.

Rodi, W. & Mackie, R.L., 2001. Nonlinear conjugate gradients algorithm for 2-D magnetotelluric inversion, *Geophysics,* **66**(1), 174–187.

Tshoso, G., 2003. Structure, chronologie et mode de mise en place du système de dykes géants de l'Okavango, Nord Botswana. Une approche pluridisclinaire, *PhD thesis*, Brest University.

van Zijl, J.S.V., 2006. A review of the resistivity structure of the Karoo Supergroup, South Africa, with emphasis on the dolerites: a study in anisotropy, *South Afr. J. Geol.,* **109,** 315–328.

Wannamaker, P.E., 1997. Tensor CSAMT survey over the Sulphur Springs thermal area, Valles Caldera, New Mexico, U.S.A. Part II: Implications from CSAMT methodology, *Geophysics,* **62**(2), 466–476.

Wannamaker, P.E., 2005. Anisotropy versus heterogeneity in continental solid earth electromagnetic studies: fundamental response characteristics and implications for physicochemical state, *Surv. Geophys.,* **26,** 733–765.

Wannamaker, P.E., Caldwell, T.G., Doerner, W.M. & Jiracek, G.R., 2004. Fault zone fluids and seismicity in compressional and extensional environments from electrical conductivity: the New Zealand Southern Alps and U.S. Great Basin, *Earth Planets Space,* **56**(12), 1171–1176.

Webb, S.J., 2009. Southern African tectonics from potential field interpretation, *PhD thesis*, University of the Witswatersrand, Johannesburg, South Africa.

Weckmann, U., Ritter, O. & Haak, V., 2003. A magnetotelluric study of the Damara Belt in Namibia. 2. MT phases over 90° reveal the internal structure of the Waterberg Fault/Omaruru Lineament, *Phys. Earth planet. Inter.,* **138,** 91–112.

Weidelt, P., 1999. 3-D conductivity models: implications of electrical anisotropy, in *Three-Dimensional Electromagnetics,* pp. 119–137, eds Oristaglio, M., Spies, B. & Cooper, M.R., Society of Exploration Geophysicists.